

www.acsami.org Forum Article

Geometric Optimization of Bismuth Vanadate Core—Shell Nanowire Photoanodes using Atomic Layer Deposition

Ashley R. Bielinski, Andrew J. Gayle, Sudarat Lee, and Neil P. Dasgupta*



Cite This: ACS Appl. Mater. Interfaces 2021, 13, 52063-52072



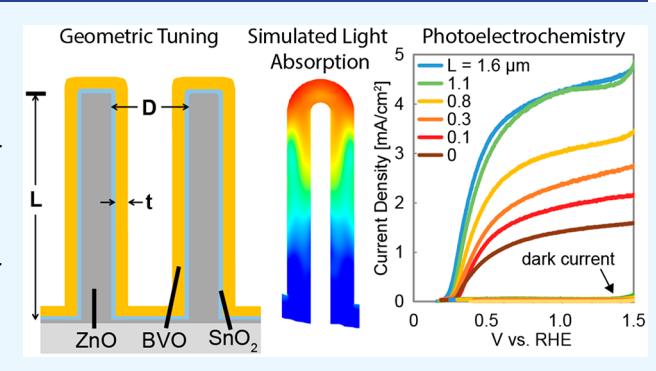
ACCESS

Metrics & More

Article Recommendations

Supporting Information

ABSTRACT: In this study, systematic geometric tuning of coreshell nanowire (NW) architectures is used to decouple the contributions from light absorption, charge separation, and charge transfer kinetics in photoelectrochemical water oxidation. Coreshell—shell NW arrays were fabricated using a combination of hydrothermal synthesis of ZnO and atomic layer deposition (ALD) of SnO₂ and BiVO₄. The length and spacing of the NW scaffold, as well as the BiVO₄ film thickness, were systematically tuned to optimize the photoelectrochemical performance. A photocurrent of 4.4 mA/cm² was measured at 1.23 V vs RHE for sulfite oxidation and 4.0 mA/cm² at 1.80 V vs RHE for water oxidation without a cocatalyst, which are the highest values reported to date for an ALD-deposited photoanode. Electromagnetic simulations demonstrate



that spatial heterogeneity in light absorption along the core—shell NW length has a critical role in determining internal quantum efficiency. The mechanistic understandings in this study highlight the benefits of systematically optimizing electrode geometry at the nanoscale when designing photoelectrodes.

KEYWORDS: photoelectrochemistry, nanowire, architected materials, modeling, geometry, photoanode, bismuth vanadate

■ INTRODUCTION

Metal oxide semiconductors are frequently used as photoanodes for photoelectrochemical (PEC) water splitting, owing to their improved stability against photocorrosion compared to Si and III-V compounds. However, metal oxide semiconductors are typically limited by wide bandgaps and poor optoelectronic properties, including a mismatch between the length scales required for complete light absorption and charge carrier diffusion.^{2,3} Nanostructuring is a common approach to overcome these optoelectronic limitations. 4,5 Nanostructures can increase light absorption through their light trapping and antireflective properties. 6,7 Additionally, their increased surface areas reduce kinetic overpotentials compared to planar geometries.² The coupled relationships between light absorption, charge transfer kinetics, and quantum efficiency are strongly dependent on the specific nanostructured geometry, 8-13 which motivates studies to optimize electrode architecture.

Nanostructures composed of the "bulk" light-absorbing semiconductor can be formed using a range of top-down or bottom-up manufacturing techniques including lithography, 14–16 wet/dry etching, 17,18 chemical vapor deposition, 19,20 and hydrothermal synthesis. 14,21 Alternatively, a semiconductor absorber layer can be deposited onto a heterogeneous template to create a core—shell structure. 22–26 The core—shell approach allows for independent control of geometry in

multiple dimensions, which enables rational design of the optical and electrochemical properties of the material system. ¹² For example, core—shell nanowires (NWs) can separate light absorption and charge carrier separation onto orthogonal directions, allowing them to be independently optimized. ^{25–27} This can be leveraged to overcome limitations in materials with mismatched optical absorption depths and carrier diffusion lengths. However, precise tuning of multiple geometric parameters including shell thickness, NW length, and inter-NW spacing is often not performed within a single study. This frequently results in a general comparison of nanostructured electrodes to planar control samples, rather than decoupling the individual influences of these geometric variables on quantum efficiency and photovoltage.

Inspiration can be taken from studies of Si NW and microwire arrays, which have been thoroughly investigated both computationally and experimentally. These studies highlight the impact of geometric features, such as NW/microwire size, 9,28 density, $^{29-31}$ and profile 9 on spectral light

Special Issue: Emerging Materials for Catalysis and Energy Applications

Received: May 19, 2021 Accepted: July 7, 2021 Published: July 20, 2021





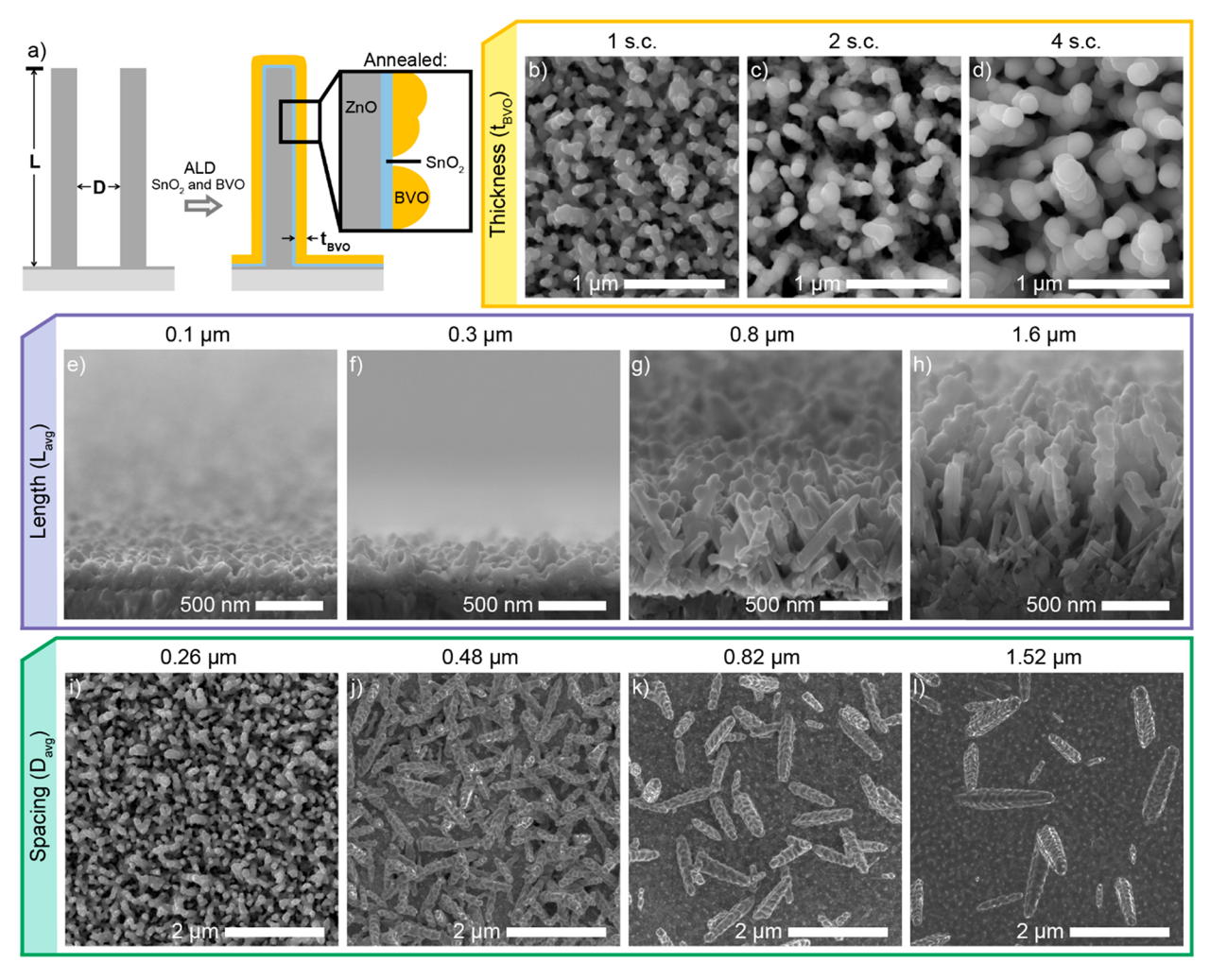


Figure 1. (a) Design parameters for a core—shell BVO NW array. (b-d) Top-down SEM images of BVO photoanodes, varying the number of supercycles (s.c), corresponding to 20, 40, and 80 nm of as-deposited ALD BVO, respectively. (e-h) Cross-sectional SEM images of photoanodes with average NW lengths from 0.1 to 1.6 μ m, with 1 s.c. of deposited BVO. (i-l) Top-down SEM images of photoanodes with average inter-NW spacing between 0.26 and 1.52 μ m, with 1 s.c. of deposited BVO. All SEM images show photoanodes after BVO annealing.

absorption, ^{9,28,30,31} surface recombination, ^{9,28,31} electrolyte mass transport, ²⁹ and reaction kinetics. ³¹ However, coreshell metal oxide NWs have material-dependent properties, advantages, and limitations that are distinct from singlematerial systems. Therefore, an improved understanding of how the core—shell NW geometry influences performance will enable rational design of optimized photoanodes.

Bismuth vanadate (BVO) is a promising photoanode material for solar water oxidation. BVO has a relatively narrow \sim 2.5 eV bandgap, ³² enabling absorption within the visible spectrum, and moderate charge carrier diffusion lengths of \sim 70 nm. ³³ Nanostructured geometries have resulted in some of the highest reported photocurrents for BVO photoanodes to date. ^{22,25,26,34–39}

In this study, a series of core—shell NW photoanodes were developed to study the influence of geometric parameters on optical properties and PEC performance. The NW geometry was chosen as a model system because of its well-defined and tunable geometric parameters, although the conclusions developed here can be extrapolated to other geometries. A template of hydrothermally grown ZnO NWs was used to tune the core geometry (length, inter-NW spacing) independently from the thickness of the BVO shell. BVO was deposited on

the NWs using atomic layer deposition (ALD), which provides conformal coverage of the NW array and enables precise control of the film composition and thickness independent of the properties of the underlying NW template. ^{22,40,41} ALD was also used to deposit an interlayer of SnO₂ between the ZnO NWs and ALD BVO, which serves a dual purpose to protect the ZnO NW from photocorrosion and serve as a hole blocking layer. ^{22,42}

As a result of the geometric optimization in this work, a maximum photocurrent of 4.4 mA/cm² was measured at 1.23 V vs RHE, which is the highest value reported to date for an ALD-deposited photoanode. External and internal quantum efficiency spectra were collected and analyzed as a function of shell thickness, NW length, and inter-NW spacing. These trends are rationalized using electromagnetic simulations, which highlight the critical role of electrode geometry on the spatial distribution of light absorption (and thus carrier excitation) throughout the NW volume. The insights from this study demonstrate how rational design of photoelectrode architectures can be used to take full advantage of the increased surface area in nanostructured electrodes, resulting in substantial increases in quantum efficiency.

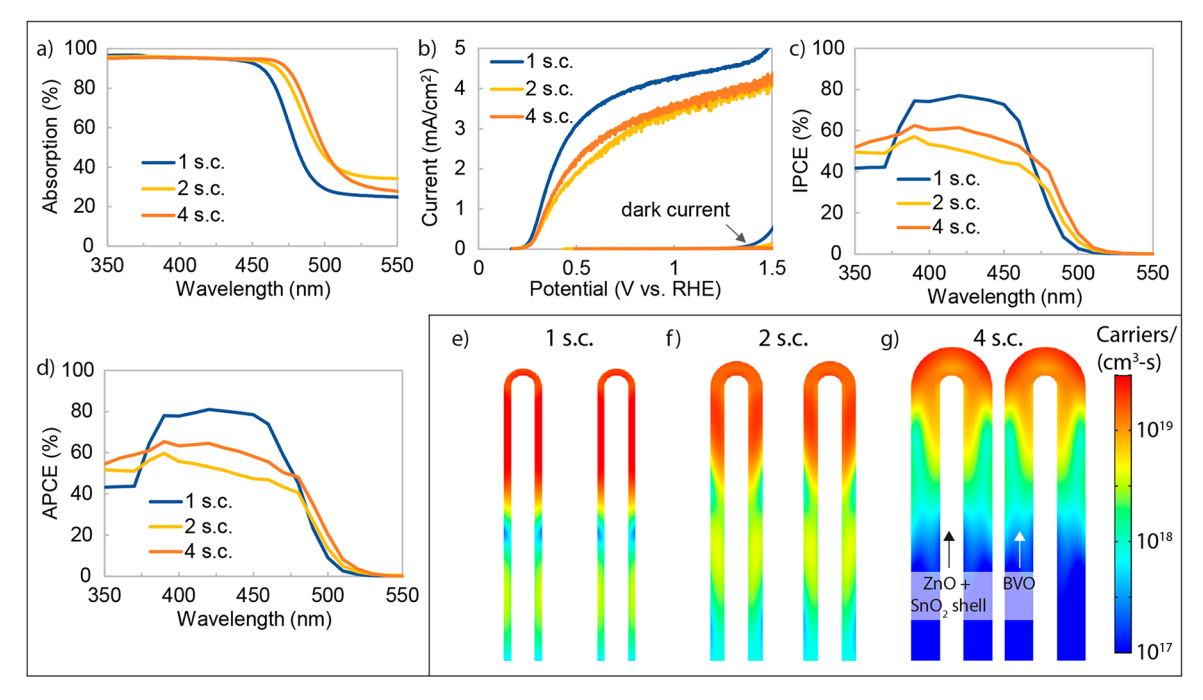


Figure 2. (a) BVO NW photoelectrode light absorption as a function of as-deposited BVO thickness. (b) Linear sweep voltammetry (LSV) for sulfite oxidation under 1-sun illumination (borate buffer, pH: 9.2). (c) IPCE and (d) APCE measurements. (e–g) Simulated carrier generation rates from a 420 nm incident plane wave source in NW arrays with 1, 2, and 4 s.c. of BVO, respectively. The upper 50% of the NWs are shown for clarity. Carrier generation rates are plotted on a logarithmic scale, given the strong gradient along the NW length.

■ RESULTS AND DISCUSSION

Tuning the Electrode Geometry. Figure 1 shows the parameters that were tuned in the ALD BVO core—shell NW photoanodes, with accompanying scanning electron microscopy (SEM) images. Geometric parameters of the ZnO NW array, such as length (L, Figure 1e-h) and average inter-NW spacing (D, Figure 1i-l), were controlled using previously developed surface-directed assembly methods. In this approach, an ALD seed layer is used to direct the nucleation of NWs, which facilitates independent control of NW angular orientation and spacing. In this thickness of the asdeposited BVO $(t_{\text{BVO}}, \text{Figure 1b-d})$ can be tuned by adjusting the number of ALD deposition cycles.

These geometric parameters act together to influence performance metrics including light absorption, charge separation, surface charge recombination, and mass transport within the electrolyte. ^{8–11,29,45,46} In a core–shell NW array, light is absorbed along the length of the NW, while charge carriers diffuse and are collected radially. ^{25–27} Thus, light absorption can be increased by lengthening the NWs without increasing the required carrier diffusion lengths.

Nanostructured geometries can also introduce new challenges. Increased surface area provides a greater number of potential reaction sites, but it may also result in increased surface and interfacial recombination. High-aspect-ratio nanostructures can also introduce concentration gradients in the electrolyte phase within the electrode.^{29,47} Furthermore, changing the nanostructure geometry (including shell thickness) can result in greater focusing of light absorption near the top of the photoelectrode, which reduces the usefulness of active surface area deeper within the electrode.^{2,46,48,49} In this study, to decouple these effects, independent control of multiple geometric parameters is used to provide fundamental insights into the factors that limit the performance of nanostructured photoelectrodes.

In ALD of ternary oxides, a supercycle (s.c.) approach is often implemented. In this method, an alternating sequence of binary oxide layers is blended within the ALD process. Film stoichiometry can be controlled by tuning the ratio of these binary oxides within the sequence. We have previously demonstrated this approach by using ALD to synthesize BVO films with tunable composition and phase. In the optimized recipe, each s.c. consists of 270 cycles of $\rm Bi_2O_3$ followed by 230 cycles of $\rm V_2O_5$. Further details on the ALD process can be found in the Experimental Section.

Variations in Shell Thickness. The first geometric parameter that was considered is shell thickness. The BVO absorber layer was deposited with varying thicknesses of approximately 20, 40, and 80 nm, corresponding to 1, 2, and 4 ALD s.c., respectively (Figure 1b–d). The average NW length was 1.6 μ m. Figure 2a shows ultraviolet—visible (UV—vis) absorption spectra for NW photoanodes with varying asdeposited BVO thicknesses. The three photoanodes each absorb approximately 95% of light intensity at wavelengths below 450 nm, while near-gap absorption at longer wavelengths increases with increasing BVO film thickness.

Figure 2b shows the photocurrent vs potential curves for sulfite oxidation in the three NW samples. Despite the increased near-gap photon absorption in the samples with the thicker shells, the NW array with the thinnest BVO shell provided the highest photocurrent. This illustrates that there was a difference in quantum efficiency for samples with varying shell thickness.

The incident photon to electron conversion efficiency (IPCE) spectra, Figure 2c, show that while external quantum efficiency improves at longer wavelengths for the thicker films, the high total photocurrent in the 1 s.c. sample is dominated by the higher IPCE over a range of wavelengths from 375 to 475 nm. The IPCE drops for wavelengths below 375 nm as shell thickness decreases, which is due to increased UV light

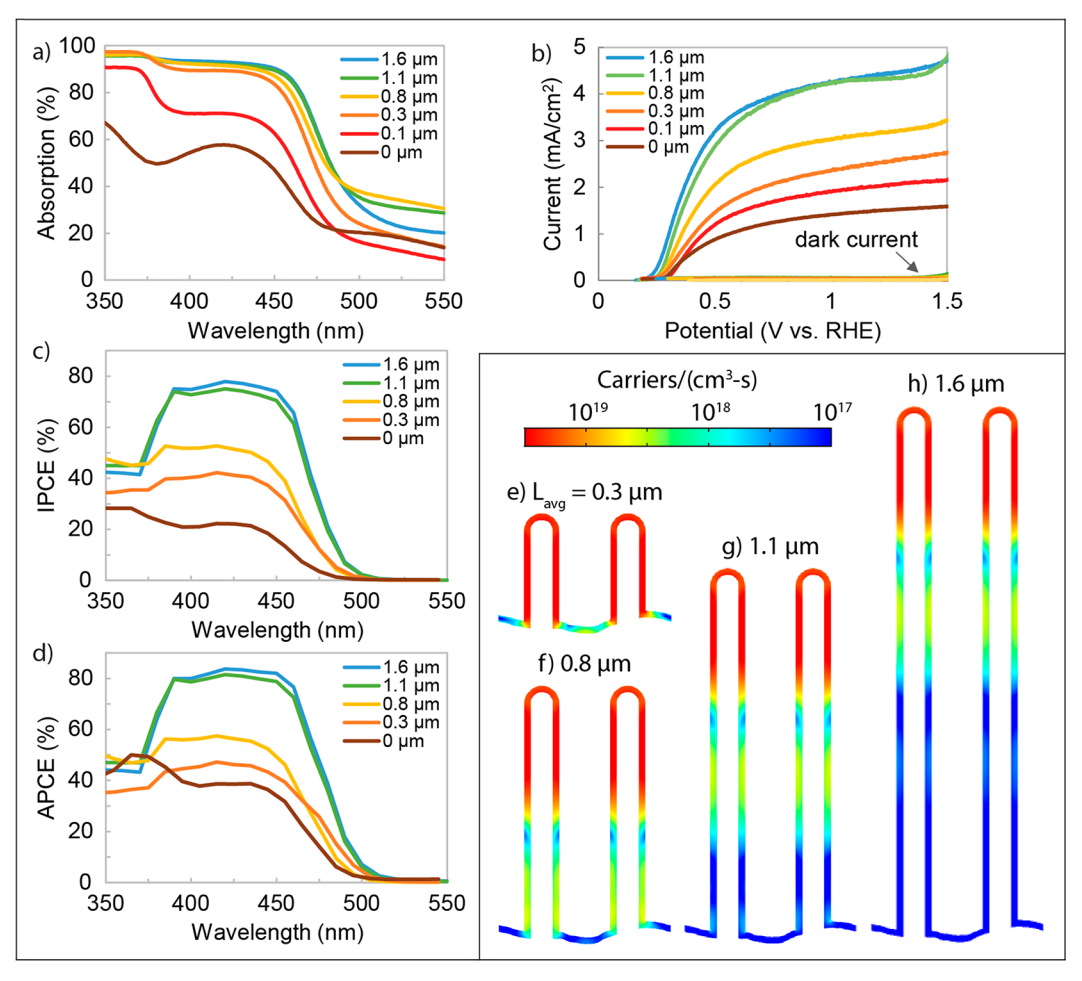


Figure 3. (a) BVO NW photoelectrode light absorption as a function of NW length. The 0 μ m sample is a planar electrode with no NWs. (b) LSV for sulfite oxidation under 1-sun illumination (borate buffer, pH: 9.2). (c) IPCE and (d) APCE measurements. (e—h) Simulated carrier generation rates from a 420 nm incident plane wave source.

absorption in the ZnO NWs (further details in Supplementary Note 9). Holes generated in the ZnO core cannot easily transfer to the BVO surface due to the valence band offset in the ZnO/SnO₂/BVO structure (Supplementary Note 3).²² However, this has a limited impact on the overall photocurrent due to the relatively low intensities in the UV region of the AM1.5G spectrum. Additionally, the absorbed photon to electron conversion efficiency (APCE) was calculated from the IPCE and light absorption data. Since all three electrodes absorb nearly 100% of the light below the bandgap, the trends in the APCE differ very little from the IPCE.

While the as-deposited BVO thickness can be controlled linearly with the number of ALD s.c., postdeposition annealing of the BVO films results in additional trends in thickness and morphology (Figure 1b-d). In all cases, the BVO forms monoclinic crystalline grains. Consistent with previous transmission electron microscopy (TEM) imaging and energy-dispersive X-ray spectroscopy (EDS) analysis, as the BVO film crystallizes, the film roughens and forms discrete grains along the NW surface. As the number of s.c. increases from 1 to 4, the shell thickness increases and the space between the NWs begins to decrease, which becomes particularly apparent in the 4 s.c. sample (Figure 1b-d). This reduces the interfacial area with the electrolyte and may result in electrolyte mass transport limitations. Furthermore, as the shell thickness increases, the required distance that

photoexcited charge carriers must diffuse increases, both in the radial direction (through the shell thickness) and in the axial direction (due to any potential pore clogging). Each of these factors would contribute to a decrease in APCE as shell thickness increases.

Beyond simply considering total light absorption by the photoelectrode, the spatial variation in light absorption within the electrode will also affect the quantum efficiency. As light absorption increases, within a specific location, the excited carrier generation rate will also increase. This will, in turn, generate a higher flux of photoexcited carriers to the electrode—electrolyte interface, which must be transferred across the interface before recombination occurs. Therefore, to probe the spatial variations in light absorption as a function of NW geometry, electromagnetic simulations [using a finite element method (FEM) solver for the frequency domain form of Maxwell's equations]⁵⁰ were performed. A complete description of this simulation method is found in ref 50.

To decrease computational cost, 2D simulations were used as a simplified model. Additionally, ALD BVO was treated as a uniform shell, which did not significantly affect the trends in absorption compared to densely spaced BVO grains (detailed methods in Supplementary Notes 6 and 16). From the simulated electric-field intensity data and photoelectrode material properties, volumetric carrier generation rates are calculated according to a previously published model: ⁵¹

$$C_{\text{gen}} = \frac{\pi |E|^2 \text{imag}(\varepsilon)}{h} \tag{1}$$

where $C_{\rm gen}$ is the carrier generation rate $(1/{\rm cm}^3/{\rm s})$, E is the simulated spatially varying electric field (V/m), imag (ε) is the spectral imaginary component of permittivity (F/m), and h is Planck's constant. Values for imag (ε) were calculated based on literature values of the real and imaginary components of the refractive index for each material (further details in Supplementary Note 6).

In Figure 2e–g, the simulated spatially varying carrier generation rates are shown for the 1, 2, and 4 BVO s.c. samples using normally incident light with a wavelength of 420 nm (additional wavelengths are shown in the Supporting Information). Although each of the three NW arrays absorb nearly all of the incident light, as the BVO thickness increases, light absorption is increasingly focused near the tips of the NWs. As a consequence of this concentrated absorption, the flux of photogenerated charge carriers are confined to a smaller active area, which will result in a higher overpotential and increased recombination rate. In addition to the mass and carrier transport phenomena described above, this optical effect further helps to rationalize the increased quantum efficiency of the 1 s.c. sample, since the flux of photogenerated carriers is more uniformly distributed along the NW length.

Overall, the shell thickness investigation points toward multiple contributing factors that must be considered when designing nanostructured photoelectrodes, including surface area, spatial distribution of light absorption, near-gap absorption, mass transport within the electrolyte, and required charge carrier diffusion length. To further decouple these effects and optimize performance, geometric variation of the NW length and spacing was performed. In these experiments, the ALD film thickness was fixed at 1 s.c. to maximize the relative photocurrent.

Variations in NW Length. The length of the NWs can influence photoelectrode performance in several ways. Longer NWs can increase total light absorption, but also have increased interfacial area. In PEC systems, increased surface and interfacial area can result in a trade-off between improved charge transfer kinetics and increased interfacial recombination. To study these effects, Figure 3a and b show the light absorption properties and photocurrent response for photoanodes with different average NW lengths ranging from 0 μ m (planar) to 1.6 μ m. Accompanying SEM images are shown in Figure 1e—h.

The light absorption above the BVO bandgap first increases with NW length and then saturates at a NW length of 0.8 μ m (Figure 3a). This is mirrored in Figures 3e-h, which show the simulated carrier generation rates at a wavelength of 420 nm. In the sample with a NW length of 0.3 μ m (Figure 3e), the NWs are not long enough to absorb all of the incident light, and a significant percentage of light is lost to transmission. The 0.8 μ m NW length (Figure 3f) is approximately the minimum height necessary to absorb all of the incident light. Extending the NW length further (Figure 3g-h) yields minimal additional absorption toward the bottom of the NWs. However, in contrast to increasing shell thickness, further increases in NW length do not result in carrier generation concentration toward the tips of the NWs. Therefore, increasing light absorption by increasing NW length is a more effective means of light management than increasing shell

thickness, since the flux of photogenerated carriers is distributed more homogeneously along the electrode surface.

The photocurrent data show a similar trend to the light absorption, where the photocurrent at a potential of 1.23 V vs RHE first increases with increasing NW length and then reaches a plateau at ~4.4 mA/cm² (Figure 3b). However, while the light absorption reaches a saturation value at a NW length of 0.8 μ m (Figure 3a), the photocurrent continues to increase until a longer NW length of 1.1 μ m. Although the photoanode only absorbs significant amounts of light along the top $\sim 0.8 \ \mu m$ of the NW length (Figure 3g-h), there is increased surface area available for the reaction deeper than this, that is, closer to the substrate. As the length increases from 0.8 to 1.1 μ m, the additional surface area at the bottom of the NWs contributes to the interfacial charge transfer reaction, which helps to explain the improved photocurrent. However, as the length of the NWs continues to increase from 1.1 to 1.6 μ m, the increase in surface area at the bottom of the NWs no longer contributes. We attribute this to the minority carrier diffusion length in BVO, which is approximately 70 nm.33 Therefore, adding more surface area in regions with minimal light absorption only contributes if the additional area is within a short diffusion distance to the locations where light absorption occurs.

In Figure 3b, the initial photocurrent onset is also shifted to slightly lower potentials as NW length increases, indicating decreased overpotentials. The reduction in overpotential corresponds to the increased surface area, providing further evidence for the benefit of extending NW length despite saturated light absorption. This is in agreement with Butler–Volmer kinetics, where the lower current density associated with increasing the electrochemically active surface area corresponds to a reduction in activation overpotential.²

Quantum efficiency measurements were performed to further investigate the impact of NW length on photocurrent (Figure 3c–d). The IPCE increases with average NW length up to 1.1 μ m, which is consistent with the increased photocurrents observed in Figure 3b. Additionally, the IPCE at longer wavelengths increases with increasing NW length, which is consistent with the near-bandgap light absorption data.

However, while a major benefit of longer NWs is overcoming light absorption limitations, the APCE data indicates that total light absorption is not the only factor contributing to the photocurrent trends. If insufficient light absorption was the only factor affecting the performance of the electrodes with different NW lengths, the APCE, which accounts only for absorbed photons, would converge for all electrodes. The fact that the APCE at a given wavelength increases from the planar geometry until the 1.1 μ m NW length indicates that the increase in APCE is correlated with the increased surface area.

The highest photocurrent at 1.23 V vs RHE was 4.4 mA/cm², which is 2.95× higher than the photocurrent for the planar control. This is the highest photocurrent for an ALD-deposited photoanode material reported to date, and represents an 1.5× increase over our previous reported value (2.9 mA/cm²), which was measured using unoptimized ALD BVO-NW architectures. On the basis of the 2.52 eV bandgap for ALD BVO²² this corresponds to 75% of the maximum theoretical photocurrent under 1 sun illumination.

In summary, increasing NW length results in coupled tradeoffs between light absorption, interfacial kinetics, carrier

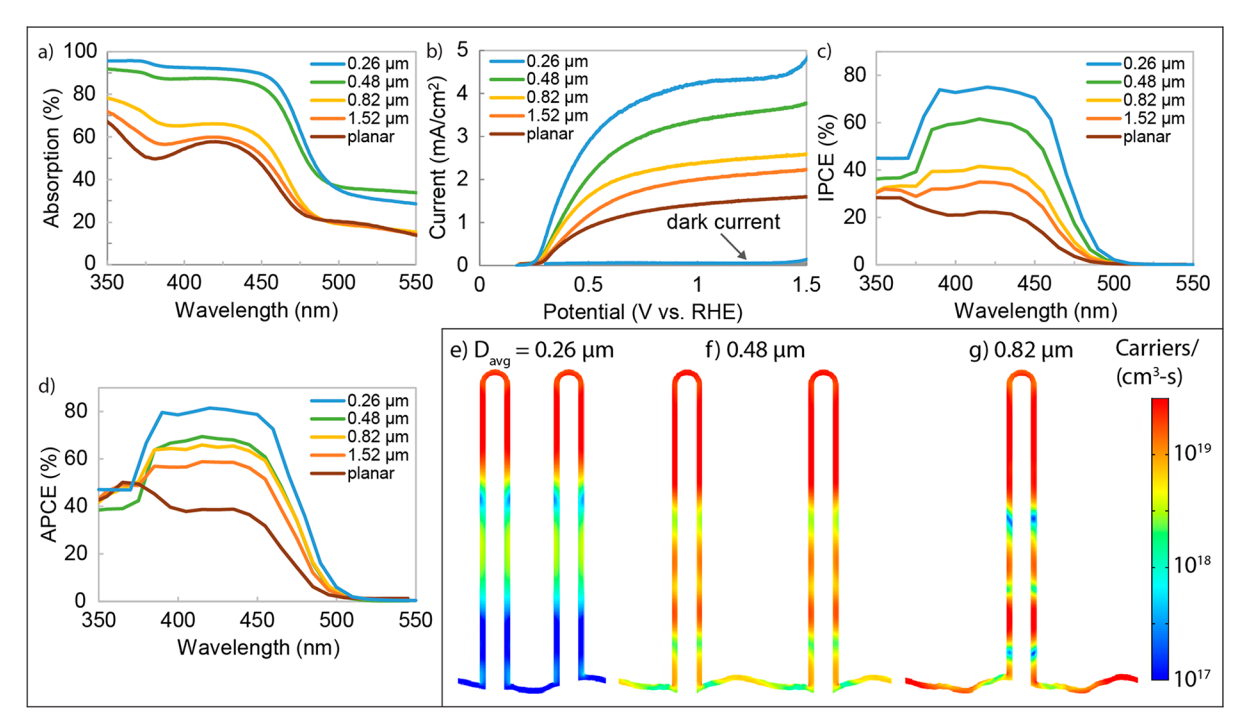


Figure 4. Samples are identified by the average NW spacing. (a) BVO NW photoelectrode light absorption as a function of average NW spacing. (b) LSV for sulfite oxidation under 1-sun illumination (borate buffer, pH 9.2). (c) IPCE and (d) APCE measurements. (e–g) Simulated carrier generation rates from a 420 nm incident plane wave source.

recombination, and charge transport along the NW length. To further decouple these variables, we explored independent control of inter-NW spacing as an additional design parameter. Varying the inter-NW spacing offers the ability to tune surface area and light absorption without changing NW length, and also allows us to study if mass transport limitations occur in the electrolyte by varying the open volume within the electrode. ^{29,47}

Variations in Inter-NW Spacing. Core—shell BVO photoanodes were grown on NW arrays with varying spacing, D, as shown in Figure 1a. The NW spacing was controlled using a submonolayer ALD ${\rm TiO_2}$ overcoat on top of the ALD ${\rm ZnO}$ seed layer, which inhibits NW nucleation during hydrothermal synthesis. This allowed the average inter-NW spacing to be monotonically increased from 0.26 to 1.52 μ m. Quantification of the NW density and inter-NW spacing is included in Supplementary Note 2. Accompanying SEM images for each of the arrays with different average NW spacings are shown in Figure 1i—l.

Figure 4a and b shows the light absorption and photocurrent data for these photoanodes. The arrays with the lowest average spacing, 0.26 μ m, correspond to the same spacing of the samples used in Figures 2 and 3. The NW length was maintained at approximately 1.1 μ m and a shell thickness of 1 s.c. of BVO was deposited in each case.

Both the light absorption and photocurrent values, Figure 4a and b, decrease as the inter-NW spacing increases. For large inter-NW spacings, substantial planar regions of the substrate are exposed to the electrolyte between the NWs. Consequently, as the inter-NW spacing increases, the photocurrent converges to that of the planar geometry.

As expected, the IPCE data (Figure 4c) follow the trend observed in the photocurrent measurements. However, the APCE data (Figure 4d) show a relatively smaller variation as a function of inter-NW spacing. The smaller differences in APCE

as a function of inter-NW spacing indicate that in these samples, total light absorption is a significant factor in determining photocurrent. Furthermore, the fact that the APCE does not increase as inter-NW spacing increases indicates that under these conditions, mass transport in the electrolyte is not a limiting factor. These APCE data can be contrasted with the trends of increasing NW length (Figure 3d), where APCE was a stronger function of length.

One potential contributing factor to these observations is the fact that surface area increases for both increasing NW length and decreasing inter-NW spacing. However, the reduction in surface area as NW length decreases is smaller in magnitude than the change in surface area as inter-NW spacing increases. This is because NW surface area scales linearly with NW length, while it scales quadratically with inter-NW spacing. Therefore, a larger inter-NW spacing results in a faster decrease in surface area than reducing the NW length. Estimations of the total surface area for each electrode geometry investigated in this study are calculated in Supplementary Note 2.

For example, as the average NW length is reduced from 1.1 to 0.8 μ m, the total surface area decreases by ~24%. As described above, this decrease in surface area results in a decrease in APCE as NW length is reduced, even though the total light absorption did not change. In contrast, as inter-NW spacing increases from 0.26 to 0.48 μ m, the electrode surface area decreases by ~48%. This decrease in surface area is even more amplified in the case of a spacing of 0.82 μ m, which represents a decrease in surface area by ~73%. Despite these dramatic changes in surface area, the APCE decreases by <20% as the inter-NW spacing is increased from 0.26 to 0.82 μ m, which is significantly less than the APCE drop as NW length decreases below 1.1 μ m (as shown in Figure 3d). Even in the extreme case when the inter-NW spacing was increased to 1.52

 μ m, representing a reduction in surface area by ~82%, the APCE only decreases by ~25%.

To reconcile the differences in APCE when tuning NW length and spacing, we examine the simulated carrier generation rate maps in Figure 4e-g. As the inter-NW spacing increases, light absorption is distributed more uniformly along the NW length. Therefore, the reduction in surface area is somewhat compensated for by a more homogeneous carrier generation rate along the length. This is analogous to the trends observed with changing shell thickness, where reduced light focusing near the NW tips increases APCE. Therefore, we conclude that an optimized geometry for nanostructured photoanodes is one that simultaneously maximizes light absorption and optimizes active surface area, which requires a homogeneous carrier generation rate throughout the electrode volume. This highlights the importance of balancing the flux of light absorption and interfacial charge transfer kinetics in PEC systems, and demonstrates the power of rational design of geometry to optimize performance.

OER Performance. While the data shown in Figures 2–4 were collected for sulfite oxidation, it is also interesting to examine the performance of these optimized NW arrays for the oxygen evolution reaction (OER). Figure 5 shows a

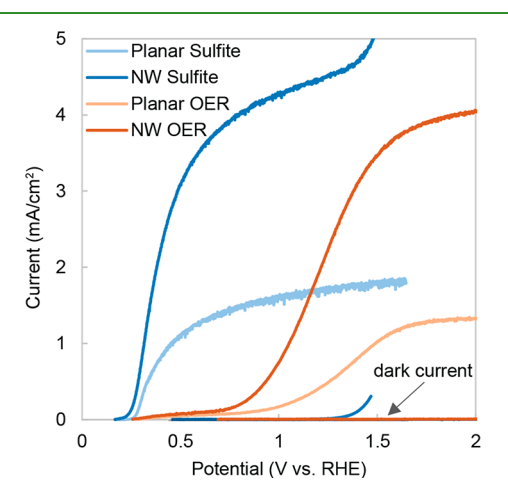


Figure 5. Comparison of water oxidation and sulfite oxidation LSV for planar and optimized NW BVO photoelectrodes.

comparison of the photocurrent versus potential response for sulfide oxidation and OER using the optimized photoelectrode geometry (1.1 μ m NW length, 0.26 μ m inter-NW spacing, and 1 s.c. BVO shell thickness). These measurements were performed without using an OER cocatalyst, which results in higher overpotentials, since the charge transfer kinetics for OER are significantly slower than those for sulfite oxidation. This can be seen in the more anodic onset of photocurrent for OER. However, despite this increased overpotential, the saturated photocurrent for OER (4.0 mA/cm² at 1.80 V vs RHE) is similar to that of sulfite oxidation. This indicates that an optimized NW geometry would perform well if paired with an appropriate OER cocatalyst, which will be the subject of future studies.

CONCLUSIONS

In this study, the impacts of geometry were investigated on the PEC performance of core-shell-shell BVO@SnO₂@ZnO NW photoanodes fabricated by ALD. The NW design parameters studied include BVO shell thickness, NW length,

and inter-NW spacing, which were independently varied to investigate their impact on performance. Optical modeling was performed to develop a mechanistic understanding of the experimental trends observed when varying each geometric parameter. The optimized geometry resulted in a sulfite oxidation photocurrent of 4.4 mA cm $^{-2}$ at 1.23 V vs RHE, which is 75% of the maximum theoretical photocurrent under 1 sun illumination.

The key points of understanding that arise from tuning the geometry are as follows:

- (1) As shell thickness increases, light absorption focuses near the tips of the NWs. This results in a high local carrier generation rate, which does not take full advantage of the increased surface area from the NW geometry. Therefore, shell thickness should be optimized to maximize the homogeneity of carrier generation throughout the electrode volume.
- (2) Increasing NW length can enhance total light absorption until a saturation value is achieved. Further increases in NW length beyond this point result in improvements in photocurrent and APCE up to a certain point, beyond which diminishing returns exist. This is attributed to the minority carrier diffusion length in the absorber layer, which limits the distance photoexcited carriers can travel to take advantage of the increased surface area as NW length increases.
- (3) Increasing inter-NW spacing results in a decrease in photocurrent, if light absorption becomes limiting. Ultimately, this strategy converges to a planar electrode geometry. However, the reduction in electrode surface area associated with increasing NW spacing can be somewhat compensated for by an improvement in homogeneity of light absorption along the NW length. This acts to spread out the flux of photogenerated carriers more uniformly. Therefore, although the total surface area is an important factor to PEC performance, it must be normalized by the homogeneity of the carrier generation rate along the surface.

In the future, the lessons learned from this study provide broadly applicable guidelines to further improvements in the performance of nanostructured photoelectrodes. For example, in materials with longer carrier diffusion lengths, increases in surface area beyond the point of saturated light absorption may be beneficial to a greater extent, since the photogenerated carriers can "take advantage of" this increased surface area. In addition, optical modeling is a powerful tool to optimize geometry to identify architectures that simultaneously maximize surface area and light absorption, while also ensuring a homogeneous distribution of carrier generation throughout the volume. Beyond the 2-D NW geometry, hierarchical architectures, such as branched NWs,43 present additional opportunities for rational design. Finally, it is important to consider the kinetic "demands" on the interface, which will become increasingly challenging for multielectron charge transfer reactions beyond water splitting. These kinetic limitations will essentially modulate the needs for increased surface area, suggesting that the optimal geometry will vary for a specific reaction. Our hope is that the fundamental insights provided in this study can provide inspiration and guidance to future studies, in particular by highlighting the critical role of heterogeneity in local light absorption and current density as a function of electrode geometry.

■ EXPERIMENTAL SECTION

Sample Preparation. Substrate Preparation. ZnO NWs were grown on fluorine-doped tin oxide on glass (FTO, Delta Technologies, $R_{\rm s} \leq 14 \ \Omega$). FTO was solvent-cleaned by sonicating in acetone, isopropanol $(2\times)$, and DI water $(3\times)$ for 10 min each. Immediately prior to ALD, substrates were cleaned using air plasma for 10 min (Harrick Plasma, PDC-001-HP). The plasma power was 10.2 W and the pressure was ∼100 mTorr.

Atomic Layer Deposition. ALD of BVO, SnO2, ZnO, and TiO2 were performed as detailed by previous publications. ^{22,43} A custom lab-built, hot-walled, cross-flow ALD reactor⁵² was used for all depositions. The precursors for ALD BVO were vanadium(V) oxytriisopropoxide (VTIP, Sigma-Aldrich), Bi(OCMe₂iPr)₃, and DI water. The precursor source temperatures were 55 and 90 °C for VTIP and Bi(OCMe2iPr)3, respectively. The DI water source was maintained at room temperature in all ALD depositions. To assist with precursor mass transport to the ALD chamber, a vapor boost strategy was used in BVO depositions (details in ref 21). SnO₂ was deposited using tetrakis(dimethylamino)tin(IV) (TDMASn) and DI water as precursors. ZnO was deposited using diethylzinc (DEZ) and DI water as precursors. TiO2 was deposited using tetrakis-(dimethylamido)titanium (TDMAT) and DI water as precursors. The source temperatures for TDMASn and TDMAT were 65 and 75 °C, respectively. The DEZ source was unheated. In all ALD recipes, purging was performed using Ultra High Purity Ar (99.999%). The deposition temperature was 175 °C for TiO₂ depositions, and 150 °C for all other materials.

Post-Annealing of ALD Films. Postannealing of both BVO and SnO₂ was performed at 450 °C in air using a tube furnace. For annealing BVO films, the ramp time was 30 min, followed by a hold for 2 h, and natural cooling lasting ~1.5 h. SnO₂ films were annealed using a ramp time of 85 min, followed by a hold for 15 min, and natural cooling lasting ~1.5 h.

Hydrothermal Nanowire Synthesis. ZnO NW synthesis used ALD ZnO and TiO2 to control nucleation and direct inter-NW spacing, as detailed in Bielinski et al. 2017.⁴³ NW growth was performed at 90 °C. The NW growth solution contained zinc nitrate hexahydrate (25 mM), hexamethylenetetramine (25 mM), and polyethylenimine (5 mM) in DI water. All substrates were faced downward to prevent settlement of homogeneous precipitates in the growth solution. NW length was controlled by adjusting the hydrothermal growth time from 0 to 2 h.

Materials Characterization. Scanning Electron Microscopy. SEM images collected on a FEI Nova 200 Nanolab with a 3 kV accelerating voltage or a TESCAN MIRA3 or TESCAN RISE with a 10 kV accelerating voltage.

Ultraviolet-Visible Spectrophotometry (UV-vis). UV-vis measurements were performed using a Schimadzu UV-2600 UV-vis Spectrophotometer with an integrating sphere. Reflectance spectra were referenced to BaSO₄, and transmittance spectra were referenced to bare FTO. The absorption (%) was calculated from the measured transmittance and reflectance using eq 2:

$$A(\%) = 100\% - T(\%) - R(\%) \tag{2}$$

Photoelectrochemical Measurements. PEC measurements were performed as detailed by Bielinski et al. 2019.²² To fabricate photoelectrodes, silver paint (Ted Pella) was used to attach a tinned-copper wire to exposed FTO on the surface. The wire connection was sealed with inert epoxy (Hysol EA, Loctite) while leaving $\sim 0.6-0.7$ cm² of active area on the electrode. The epoxy was allowed to cure for 24 h at room temperature. For PEC measurements, a quartz three-electrode cell was used. The reference electrode was Ag/AgCl immersed in 3 M NaCl (CH Instruments) and the counter electrode was a Pt wire (23 cm, CH Instruments). The electrolyte for the sulfite oxidation experiments was an aqueous solution of 1 M Na₂SO₃ (ACS Reagent, Sigma-Aldrich) and 0.25 M potassium borate buffered at pH 9.2 (Sigma-Aldrich). The electrolyte used for the OER experiments included the same borate buffer (pH 9.2) without the addition of Na₂SO₃. An Interface 1000 Potentiostat

(Gamry) was used to gather linear sweep voltammogram (LSV) data. The light source was a 300 W Xe arc lamp (Newport) equipped with an AM1.5G filter (Newport) and a quartz diffuser (Newport). Frontside illumination was performed at an intensity of 1 sun. Additional information about PEC measurements, including pH measurement and incident light calibration, iR compensation, and IPCE/APCE data collection and calculations are detailed in Supplementary Note 4.

ASSOCIATED CONTENT

Supporting Information

The Supporting Information is available free of charge at https://pubs.acs.org/doi/10.1021/acsami.1c09236.

Additional top-down and cross-sectional SEM, electrode stability measurements, NW geometry calculations, PEC experimental details, optical simulations methods, simulated electric field intensity and carrier generation plots at different wavelengths, simulated absorption spectra, comparison of simulations with discrete grains of BVO and angled NWs, and tabulated PEC responses for BVO photoanodes (PDF)

AUTHOR INFORMATION

Corresponding Author

Neil P. Dasgupta - Department of Mechanical Engineering and Department of Materials Science and Engineering, University of Michigan, Ann Arbor, Michigan 48109, United States; orcid.org/0000-0002-5180-4063; Email: ndasgupt@umich.edu

Authors

Ashley R. Bielinski – Department of Mechanical Engineering, University of Michigan, Ann Arbor, Michigan 48109, United

Andrew J. Gayle - Department of Mechanical Engineering, University of Michigan, Ann Arbor, Michigan 48109, United

Sudarat Lee - Department of Mechanical Engineering, University of Michigan, Ann Arbor, Michigan 48109, United States; orcid.org/0000-0002-0851-4626

Complete contact information is available at: https://pubs.acs.org/10.1021/acsami.1c09236

Author Contributions

[#]A.R.B, A.J.G., and S.L. contributed equally to this work.

Notes

The authors declare no competing financial interest.

ACKNOWLEDGMENTS

This work was supported by the National Science Foundation under Grant No. 1751590. A.R.B and A.J.G acknowledge support from the National Science Foundation Graduate Research Fellowship Program under Grant No. DGE-1256260. The authors acknowledge the financial support of the University of Michigan College of Engineering and technical support from the Michigan Center for Materials Characterization.

REFERENCES

(1) Hu, S.; Shaner, M. R.; Beardslee, J. A.; Lichterman, M.; Brunschwig, B. S.; Lewis, N. S. Amorphous TiO₂ Coatings Stabilize Si, GaAs, and GaP Photoanodes for Efficient Water Oxidation. Science 2014, 344 (6187), 1005-1009.

- (2) Liu, C.; Dasgupta, N. P.; Yang, P. Semiconductor Nanowires for Artificial Photosynthesis. *Chem. Mater.* **2014**, 26 (1), 415–422.
- (3) Zhang, L.; Ye, X.; Boloor, M.; Poletayev, A.; Melosh, N. A.; Chueh, W. C. Significantly Enhanced Photocurrent for Water Oxidation in Monolithic Mo:BiVO₄/SnO₂/Si by Thermally Increasing the Minority Carrier Diffusion Length. *Energy Environ. Sci.* **2016**, 9 (6), 2044–2052.
- (4) Sivula, K.; Le Formal, F.; Grätzel, M. Solar Water Splitting: Progress Using Hematite (α -Fe₂O₃) Photoelectrodes. *ChemSusChem* **2011**, *4* (4), 432–449.
- (5) Chen, S.; Thind, S. S.; Chen, A. Nanostructured Materials for Water Splitting—State of the Art and Future Needs: A Mini-Review. *Electrochem. Commun.* **2016**, *63*, 10–17.
- (6) Yu, R.; Lin, Q.; Leung, S. F.; Fan, Z. Nanomaterials and Nanostructures for Efficient Light Absorption and Photovoltaics. *Nano Energy* **2012**, *1* (1), 57–72.
- (7) Otnes, G.; Borgström, M. T. Towards High Efficiency Nanowire Solar Cells. *Nano Today* **2017**, *12*, 31–45.
- (8) Hwang, Y. J.; Hahn, C.; Liu, B.; Yang, P. Photoelectrochemical Properties of TiO₂ Nanowire Arrays: A Study of the Dependence on Length and Atomic Layer Deposition Coating. *ACS Nano* **2012**, *6* (6), 5060–5069.
- (9) Foley, J. M.; Price, M. J.; Feldblyum, J. I.; Maldonado, S. Analysis of the Operation of Thin Nanowire Photoelectrodes for Solar Energy Conversion. *Energy Environ. Sci.* **2012**, *5*, 5203–5220.
- (10) Deng, J.; Su, Y.; Liu, D.; Yang, P.; Liu, B.; Liu, C. Nanowire Photoelectrochemistry. *Chem. Rev.* **2019**, *119* (15), 9221–9259.
- (11) Dasgupta, N. P.; Sun, J.; Liu, C.; Brittman, S.; Andrews, S. C.; Lim, J.; Gao, H.; Yan, R.; Yang, P. 25th Anniversary Article: Semiconductor Nanowires—Synthesis, Characterization, and Applications. *Adv. Mater.* **2014**, *26* (14), 2137–2184.
- (12) Xiao, F.-X.; Miao, J.; Tao, H. B.; Hung, S.-F.; Wang, H.-Y.; Yang, H. B.; Chen, J.; Chen, R.; Liu, B. One-Dimensional Hybrid Nanostructures for Heterogeneous Photocatalysis and Photoelectrocatalysis. *Small* **2015**, *11* (18), 2115–2131.
- (13) Xiao, F.-X.; Miao, J.; Liu, B. Self-Assembly of Aligned Rutile@anatase TiO₂ Nanorod@CdS Quantum Dots Ternary Core—Shell Heterostructure: Cascade Electron Transfer by Interfacial Design. *Mater. Horiz.* **2014**, *1*, 259–263.
- (14) Wang, W.; Dong, J.; Ye, X.; Li, Y.; Ma, Y.; Qi, L. Heterostructured TiO₂ Nanorod@Nanobowl Arrays for Efficient Photoelectrochemical Water Splitting. *Small* **2016**, *12* (11), 1469–1478.
- (15) Lu, Y.; Lal, A. High-Efficiency Ordered Silicon Nano-Conical-Frustum Array Solar Cells by Self-Powered Parallel Electron Lithography. *Nano Lett.* **2010**, *10* (11), 4651–4656.
- (16) Yu, M.; Long, Y.-Z.; Sun, B.; Fan, Z. Recent Advances in Solar Cells Based on One-Dimensional Nanostructure Arrays. *Nanoscale* **2012**, *4*, 2783–2796.
- (17) Li, X. Metal Assisted Chemical Etching for High Aspect Ratio Nanostructures: A Review of Characteristics and Applications in Photovoltaics. *Curr. Opin. Solid State Mater. Sci.* **2012**, *16* (2), 71–81.
- (18) Ali, M.; Zhou, F.; Chen, K.; Kotzur, C.; Xiao, C.; Bourgeois, L.; Zhang, X.; MacFarlane, D. R. Nanostructured Photoelectrochemical Solar Cell for Nitrogen Reduction Using Plasmon-Enhanced Black Silicon. *Nat. Commun.* **2016**, *7*, 11335.
- (19) Shi, J.; Hara, Y.; Sun, C.; Anderson, M. A.; Wang, X. Three-Dimensional High-Density Hierarchical Nanowire Architecture for High-Performance Photoelectrochemical Electrodes. *Nano Lett.* **2011**, *11* (8), 3413–3419.
- (20) An, W.-J.; Thimsen, E.; Biswas, P. Aerosol-Chemical Vapor Deposition Method for Synthesis of Nanostructured Metal Oxide Thin Films with Controlled Morphology. *J. Phys. Chem. Lett.* **2010**, *1* (1), 249–253.
- (21) Bielinski, A. R.; Kazyak, E.; Schlepütz, C. M.; Jung, H. J.; Wood, K. N.; Dasgupta, N. P. Hierarchical ZnO Nanowire Growth with Tunable Orientations on Versatile Substrates Using Atomic Layer Deposition Seeding. *Chem. Mater.* **2015**, *27* (13), 4799–4807.

- (22) Bielinski, A. R.; Lee, S.; Brancho, J. J.; Esarey, S. L.; Gayle, A. J.; Kazyak, E.; Sun, K.; Bartlett, B. M.; Dasgupta, N. P. Atomic Layer Deposition of Bismuth Vanadate Core—Shell Nanowire Photoanodes. *Chem. Mater.* **2019**, *31* (9), 3221–3227.
- (23) Hsu, Y.-K.; Chen, Y.-C.; Lin, Y.-G. Novel ZnO/Fe₂O₃ Core—Shell Nanowires for Photoelectrochemical Water Splitting. *ACS Appl. Mater. Interfaces* **2015**, 7 (25), 14157–14162.
- (24) Coridan, R. H.; Arpin, K. A.; Brunschwig, B. S.; Braun, P. V.; Lewis, N. S. Photoelectrochemical Behavior of Hierarchically Structured Si/WO₃ Core-Shell Tandem Photoanodes. *Nano Lett.* **2014**, *14* (5), 2310–2317.
- (25) Zhou, L.; Zhao, C.; Giri, B.; Allen, P.; Xu, X.; Joshi, H.; Fan, Y.; Titova, L. V.; Rao, P. M. High Light Absorption and Charge Separation Efficiency at Low Applied Voltage from Sb-Doped SnO₂/BiVO₄ Core/Shell Nanorod-Array Photoanodes. *Nano Lett.* **2016**, *16* (6), 3463–3474.
- (26) Rao, P. M.; Cai, L.; Liu, C.; Cho, I. S.; Lee, C. H.; Weisse, J. M.; Yang, P.; Zheng, X. Simultaneously Efficient Light Absorption and Charge Separation in WO₃/BiVO₄ Core/Shell Nanowire Photoanode for Photoelectrochemical Water Oxidation. *Nano Lett.* **2014**, *14* (2), 1099–1105.
- (27) Kayes, B. M.; Atwater, H. A.; Lewis, N. S. Comparison of the Device Physics Principles of Planar and Radial P-n Junction Nanorod Solar Cells. *J. Appl. Phys.* **2005**, *97* (11), 114302.
- (28) Garnett, E.; Yang, P. Light Trapping in Silicon Nanowire Solar Cells. *Nano Lett.* **2010**, *10* (3), 1082–1087.
- (29) Xiang, C.; Meng, A. C.; Lewis, N. S. Evaluation and Optimization of Mass Transport of Redox Species in Silicon Microwire-Array Photoelectrodes. *Proc. Natl. Acad. Sci. U. S. A.* **2012**, *109* (39), 15622–15627.
- (30) Kelzenberg, M. D.; Boettcher, S. W.; Petykiewicz, J. A.; Turner-Evans, D. B.; Putnam, M. C.; Warren, E. L.; Spurgeon, J. M.; Briggs, R. M.; Lewis, N. S.; Atwater, H. A. Enhanced Absorption and Carrier Collection in Si Wire Arrays for Photovoltaic Applications. *Nat. Mater.* **2010**, *9*, 239–244.
- (31) Esposito, D. V.; Lee, Y.; Yoon, H.; Haney, P. M.; Labrador, N. Y.; Moffat, T. P.; Talin, A. A.; Szalai, V. A. Deconvoluting the Influences of 3D Structure on the Performance of Photoelectrodes for Solar-Driven Water Splitting. *Sustain. Energy Fuels* **2017**, *1*, 154–173.
- (32) Cooper, J. K.; Gul, S.; Toma, F. M.; Chen, L.; Liu, Y.-S.; Guo, J.; Ager, J. W.; Yano, J.; Sharp, I. D. Indirect Bandgap and Optical Properties of Monoclinic Bismuth Vanadate. *J. Phys. Chem. C* **2015**, 119 (6), 2969–2974.
- (33) Abdi, F. F.; Savenije, T. J.; May, M. M.; Dam, B.; Van De Krol, R. The Origin of Slow Carrier Transport in BiVO₄ Thin Film Photoanodes: A Time-Resolved Microwave Conductivity Study. *J. Phys. Chem. Lett.* **2013**, *4* (16), 2752–2757.
- (34) Bera, S.; Lee, S. A.; Lee, W.-J.; Kim, J.-H.; Kim, C.; Kim, H. G.; Khan, H.; Jana, S.; Jang, H. W.; Kwon, S.-H. Hierarchical Nanoporous BiVO₄ Photoanodes with High Charge Separation and Transport Efficiency for Water Oxidation. ACS Appl. Mater. Interfaces 2021, 13 (12), 14291–14301.
- (35) Shi, X.; Choi, I. Y.; Zhang, K.; Kwon, J.; Kim, D. Y.; Lee, J. K.; Oh, S. H.; Kim, J. K.; Park, J. H. Efficient Photoelectrochemical Hydrogen Production from Bismuth Vanadate-Decorated Tungsten Trioxide Helix Nanostructures. *Nat. Commun.* **2014**, *5*, 4775.
- (36) Kuang, Y.; Jia, Q.; Nishiyama, H.; Yamada, T.; Kudo, A.; Domen, K. A Front-Illuminated Nanostructured Transparent BiVO₄ Photoanode for > 2% Efficient Water Splitting. *Adv. Energy Mater.* **2016**, *6* (2), 1501645.
- (37) Kim, T. W.; Choi, K.-S. Nanoporous BiVO₄ Photoanodes with Dual-Layer Oxygen Evolution Catalysts for Solar Water Splitting. *Science* **2014**, 343 (6174), 990–994.
- (38) Ma, Z.; Song, K.; Wang, L.; Gao, F.; Tang, B.; Hou, H.; Yang, W. WO₃/BiVO₄ Type-II Heterojunction Arrays Decorated with Oxygen-Deficient ZnO Passivation Layer: A Highly Efficient and Stable Photoanode. ACS Appl. Mater. Interfaces 2019, 11 (1), 889–897.

- (39) Tang, Y.; Wang, R.; Yang, Y.; Yan, D.; Xiang, X. Highly Enhanced Photoelectrochemical Water Oxidation Efficiency Based on Triadic Quantum Dot/Layered Double Hydroxide/BiVO₄ Photoanodes. ACS Appl. Mater. Interfaces **2016**, 8 (30), 19446–19455.
- (40) George, S. M. Atomic Layer Deposition: An Overview. *Chem. Rev.* **2010**, *110* (1), 111–131.
- (41) Cremers, V.; Puurunen, R. L.; Dendooven, J. Conformality in Atomic Layer Deposition: Current Status Overview of Analysis and Modelling. *Appl. Phys. Rev.* **2019**, *6* (2), 021302.
- (42) Lamm, B.; Zhou, L.; Rao, P.; Stefik, M. Atomic Layer Deposition of Space-Efficient SnO₂ Underlayers for BiVO₄ Host—Guest Architectures for Photoassisted Water Splitting. *ChemSusChem* **2019**, *12* (9), 1916–1924.
- (43) Bielinski, A. R.; Boban, M.; He, Y.; Kazyak, E.; Lee, D. H.; Wang, C.; Tuteja, A.; Dasgupta, N. P. Rational Design of Hyperbranched Nanowire Systems for Tunable Superomniphobic Surfaces Enabled by Atomic Layer Deposition. ACS Nano 2017, 11 (1), 478–489.
- (44) Wang, J.; Lee, S.; Bielinski, A. R.; Meyer, K. A.; Dhyani, A.; Ortiz-Ortiz, A. M.; Tuteja, A.; Dasgupta, N. P. Rational Design of Transparent Nanowire Architectures with Tunable Geometries for Preventing Marine Fouling. *Adv. Mater. Interfaces* **2020**, 7 (17), 2000672.
- (45) Wang, T.; Luo, Z.; Li, C.; Gong, J. Controllable Fabrication of Nanostructured Materials for Photoelectrochemical Water Splitting via Atomic Layer Deposition. *Chem. Soc. Rev.* **2014**, 43, 7469–7484.
- (46) Zhao, Y.; Balasubramanyam, S.; Bol, A. A.; Bieberle-Hütter, A. Relating the 3D Geometry and Photoelectrochemical Activity of WO₃-Loaded n-Si Nanowires: Design Rules for Photoelectrodes. *ACS Appl. Energy Mater.* **2020**, *3* (10), 9628–9634.
- (47) Kemppainen, E.; Halme, J.; Lund, P. Physical Modeling of Photoelectrochemical Hydrogen Production Devices. *J. Phys. Chem. C* **2015**, *119* (38), 21747–21766.
- (48) Rodríguez, R. E.; Agarwal, S. P.; An, S.; Kazyak, E.; Das, D.; Shang, W.; Skye, R.; Deng, T.; Dasgupta, N. P. Biotemplated Morpho Butterfly Wings for Tunable Structurally Colored Photocatalysts. *ACS Appl. Mater. Interfaces* **2018**, *10* (5), 4614–4621.
- (49) Kisch, H.; Bahnemann, D. Best Practice in Photocatalysis: Comparing Rates or Apparent Quantum Yields? *J. Phys. Chem. Lett.* **2015**, *6* (10), 1907–1910.
- (50) Wave Optics Module User's Guide, COMSOL Multiphysics, ver. 5.4; COMSOL AB: Stockholm, Sweden, 2018.
- (51) Shaner, M. R.; Fountaine, K. T.; Ardo, S.; Coridan, R. H.; Atwater, H. A.; Lewis, N. S. Photoelectrochemistry of Core—Shell Tandem Junction n-P+-Si/n- WO₃Microwire Array Photoelectrodes. *Energy Environ. Sci.* **2014**, *7*, 779—790.
- (52) Dasgupta, N. P.; Mack, J. F.; Langston, M. C.; Bousetta, A.; Prinz, F. B. Design of an Atomic Layer Deposition Reactor for Hydrogen Sulfide Compatibility. *Rev. Sci. Instrum.* **2010**, *81* (4), 044102.